The 2006 Eruption of Augustine Volcano, Alaska
Power, J.A., Coombs, M.L., and Freymueller, J.T., editors
U.S. Geological Survey Professional Paper 1769

Chapter 24

Imaging Observations of Thermal Emissions from Augustine Volcano Using a Small Astronomical Camera

By Davis D. Sentman[1], Stephen R. McNutt[1], Hans C. Stenbaek-Nielsen[1], Guy Tytgat[2], and Nicole DeRoin[1]

Abstract

Long-exposure visible-light images of Augustine Volcano were obtained using a charge-coupled device (CCD) camera during several nights of the 2006 eruption. The camera was located 105 km away, at Homer, Alaska, yet showed persistent bright emissions from the north flank of the volcano corresponding to steam releases, pyroclastic flows, and rockfalls originating near the summit. The apparent brightness of the emissions substantially exceeded that of the background nighttime scene. The bright signatures in the images are shown to probably be thermal emissions detected near the long-wavelength limit (~1 μm) of the CCD. Modeling of the emissions as a black-body brightness yields an apparent temperature of 400 to 450°C that likely reflects an unresolved combination of emissions from hot ejecta and cooler material.

Introduction

Augustine Volcano is one of a chain of 80 Alaskan/Aleutian volcanoes of which 41 have been historically active (see Power and Lalla, this volume). Augustine, the most active of the Cook Inlet volcanoes, erupted previously in 1812, 1883, 1935, 1964, 1976, and 1986. Volcanic plumes, which are well known to be accompanied by lightning and other atmospheric electrical phenomena (James and others, 2008) have recently been the subject of several studies (McNutt and Davis, 2000; Williams and McNutt, 2005; McNutt and Williams, 2010). Recent volcanic activity has permitted a wide range of new studies to be undertaken, including volcanic lightning (Thomas and others, 2007 this volume), infrasound both locally (see McNutt and others, this volume) and at regional distances (Olson and others, 2006), and low-light nighttime imaging. Preliminary imaging observations of volcanic lightning that were attempted during the Augustine eruption in early 2006 are the subject of this chapter.

An increase in seismic activity beneath the mountain began on April 30, 2005 (see Jacobs and McNutt, this volume), eventually reaching high enough levels to lead to the Alaska Volcano Observatory issuing a color-code change to yellow in November 2005 and, finally, to a series of explosive eruptions beginning in January 2006 (see Power and Lalla, this volume). After the initial explosions on January 11, 13, and 14, a small astronomical camera was deployed with the intention of capturing images of lightning associated with the volcanic plume, such as those detected in radio emissions and described by Thomas and others (this volume). After the camera deployment on January 21, two large explosions occurred on January 27 and 28 that pushed ash plumes to at least 9 km above sea level, but adverse weather prevented observations of these explosions. No other large explosive eruptions occurred during the deployment interval of January 21 to April 15 that may have been accompanied by lightning, and no lightning was detected during our observations. However, faint nocturnal optical emissions associated with steam releases, rockfalls, and pyroclastic flows were unexpectedly observed with the imaging system that were associated with seismic activity measured from instruments on the island. Here we describe the imaging experiment that recorded these new data, with an analysis indicating that the detected emissions are most likely near-infrared (NIR) thermal emissions registered near the upper wavelength sensitivity limit (1.1 μm) of the camera charge-coupled device CCD.

[1]Geophysical Institute, 903 Koyukuk Drive, University of Alaska Fairbanks, Fairbanks, AK 99775.

[2] 2IRIS PASSCAL Instrument Center, New Mexico Tech, 100 East Road, Socorro, NM 87801.

Observations

Location and Geometry Relative to Augustine Volcano

Observations were made from the University of Alaska's Homer field site (lat 59.658° N., long 151.652° W.), which sits atop a 200-m-high bluff overlooking Cook Inlet to the west. During clear weather the location permits an unobstructed view of Augustine Volcano (lat 59.367° N., long 153.430° W.) at a distance of ~105 km west-southwestward across the open water of the inlet. Geophysical monitoring stations located on the island were described by DeRoin and others (2007), McNutt and others (this volume), and Power and Lalla (this volume).

Imaging System

The imaging observations were made using a monochrome Starlight Xpress model SXV-M7 16-bits/pixel integrating astronomical camera with a USB 2.0 external interface. The camera uses a 1/2 inch format Sony ICX429ALL monochrome 752- by 582-pixel CCD array, with pixel dimensions 8.6.by 8.3 μm, and a single stage of unregulated Peltier cooling to reduce thermal noise. The EXview Hole Accumulation Diode (HAD) technology used in this class of silicon sensors exhibits an extended wavelength response, with some sensitivity to 1.1 μm. This is in the near-infrared (NIR) wavelength range, slightly beyond the range of human eyesight (0.4–0.7 μm).

Various standard C-mount lenses were tested during the experiment, but the lenses used for most observations were a Tamron 35 mm f/2.4 CCTV (11.0° by 8.2° field of view, 26.6-m/pixel resolution at the observing distance of 105 km to Augustine Island) and a Sigma 135 mm f/1.8 (2.85° by 2.0° field-of-view, 6.89-m/pixel resolution at Augustine Volcano). Images were typically obtained at 10–20 s intervals, with a 5 to 15 s integration times, followed by 5 s image readout to a USB 2.0 disk drive and pause to wait for the next open-shutter synchronization command. Images were saved in 16-bit Flexible Image Transport System (FITS) format, which also recorded the start time of image integration. Camera operations were controlled using a custom script running within Cyanogen Inc.'s MaxIM DL/CCD v4 software operating under Microsoft Windows XP on an IBM notebook computer. The imaging system was connected to the Internet and remotely controlled from Fairbanks by way of Windows Remote Desktop operating over a virtual private network (VPN). System time was maintained accurate to ~100 ms by way of Network Time Protocol (NTP), which was deemed to be sufficiently accurate for correlation with other types of Augustine observations. Image collection commenced shortly after local sundown and continued uninterruptedly until sunrise the following morning, with 2,000 to 3,000 images typically recorded each night. The images were downloaded over the Internet each morning for archiving and offline analysis.

Sample Images

During the early part of the observing campaign (January 21 to February 12, 2006) a 35 mm f/2.4 wide-angle (11.0° by 8.2°) lens was used for the observations. In one scene, recorded the night of February 8 (UTC; fig. 1), Augustine is visible in the lower midcenter, with bright emissions emanating from along its north (right) flank.

Figure 1 records the broadband brightness detected by the monochrome camera at each pixel in the scene and has been colorized to aid interpretation. As shown below, the bright emissions labeled "NIR thermal emissions" appear to originate in the black-body emission spectrum of a hot source and are detectable because of the NIR sensitivity of the CCD. The other features in the image, such as cirrus haze, stars, reflected moonlight from the waters of Cook Inlet, and the foreground moonlit snowfield, provide the context needed to interpret the image, including the ability to spatially locate the source of the thermal emissions relative to Augustine Volcano and meteorological information needed to determine the quality of the viewing conditions (snow, fog, wind, and so on).

During most of the observing campaign (February 13 to April 15, 2006) a 135 mm f/1.8 lens with a narrow field of view (2.85° by 2.0°) was used for the observations. A second sample image, recorded on March 15 shortly after sunset, is shown in figure 2. Here, a steam plume is visible, along with several small thermal emissions near the summit and along the right (north) flank of the volcano.

Because thermal imaging of hot sources is commonly performed using infrared cameras with sensing elements optimized for the the most intense thermal emission wavelengths, we were surprised to see thermal-emissions with a silicon-based CCD. Imagers in satellite systems (Dehn and others, 2002) or in forward looking infrared (FLIR) cameras (Calvari and others, 2005; Harris and others, 2005; Patrick and others, 2007) for detecting the thermal activity associated with terrestrial volcanoes generally utilize non-silicon technology. However, CCD imaging has been used to investigate the active volcanism on Jupiter's moon Io (McEwen and others, 1997), and the CCD camera aboard the Galileo spacecraft was able to detect brightness temperatures down to ~700 K (430°C) in panchromatic images, although 1,000 K (730°C) was a more practical limit. Tighter temperature constraints came from images at different wavelengths, which allowed color temperatures to be computed (McEwen and others, 1998; Radebaugh and others, 2004; Milazzo and others, 2005; Keszthelyi and others, 2007). The coincidence of the transient, bright emission features recorded in our images with the seismic activity simultaneously recorded by instruments located on the volcanic island (DeRoin and others, 2007) strongly suggested that the bright features were thermal emissions

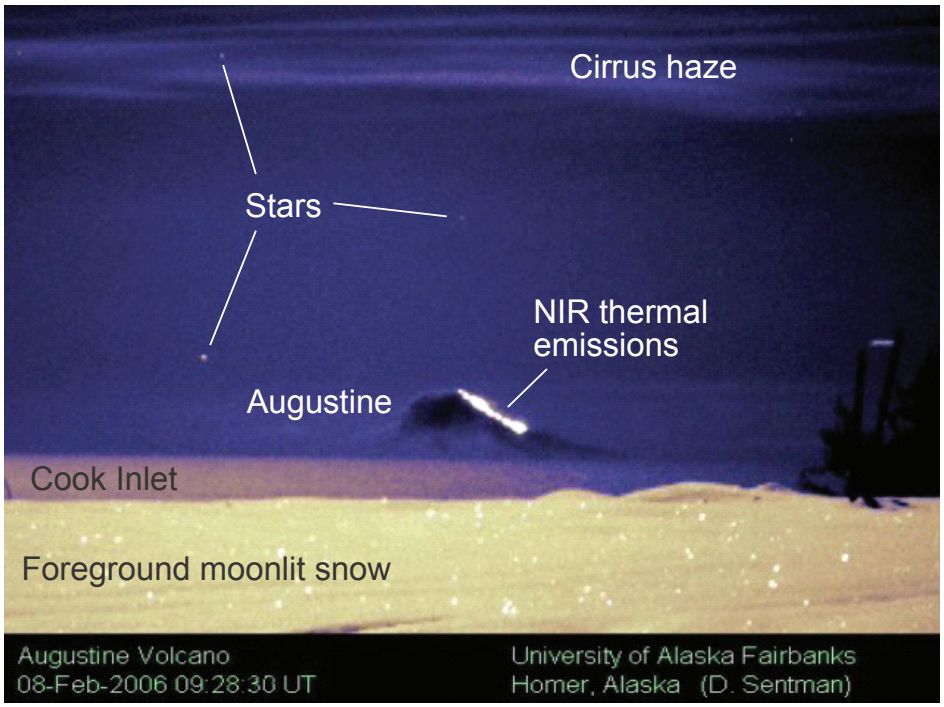

Figure 1. Augustine Volcano as observed the night of February 8, 2006 (UTC), from Homer, Alaska, when a bright moon illuminated the scene, including the steam from left (south) downwind side of the volcano. The image has been contrast stretched and colorized to facilitate feature identification.

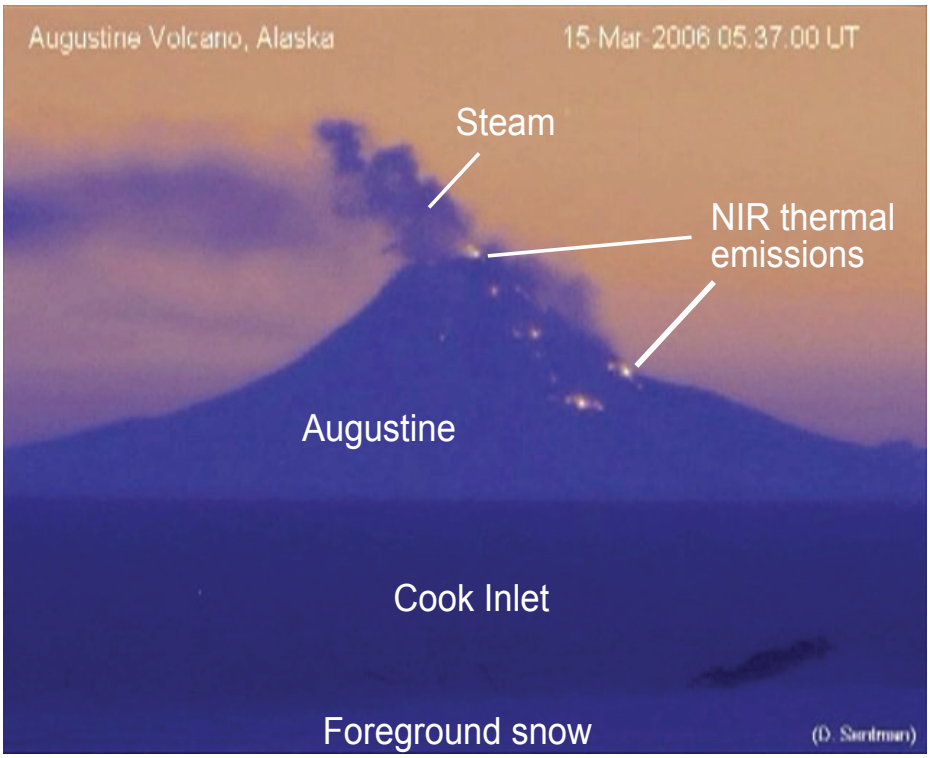

Figure 2. A zoomed image of Augustine obtained on March 15, 2006 (UTC), soon after local sunset using a 135 mm f/1.8 lens. As with figure 1, a false color palette has been used.

from pyroclastic flows or other hot ejecta. This prompted an analysis of the response of the camera to black-body thermal emissions with the aim of obtaining a general understanding of the various factors that enter into the analysis and ascertaining whether such observations might be useful as part of a more general program of volcano monitoring.

Analysis—Detectability of Thermal Emissions

The detectability of thermal emissions from a natural source depends on a combination of the source emission spectrum, the atmospheric radiative transfer characteristics between the source and the observer, the transfer function of the optical train in the sensor system, and the spectral response of the detector. For a silicon CCD detector, the measurements consist of the number of photons from the source emission spectrum that survive atmospheric absorption and losses in the optical train and within the sensor. To be a statistically meaningful observation, photon counts also must significantly exceed internal thermal and read noise associated with the sensor itself. Below we consider these factors in order.

Planck Black-body Emission Spectrum

Assuming that the bright emissions observed are black-body thermal emissions, Wien's displacement law relating the wavelength λ_{max} of peak emissions in the Planck radiation curve and the temperature T is $\lambda_{max} T = 2897\ \mu$m K, and so for a nominal temperature $T = 1{,}000$K we have $\lambda_{max} = 2.897\ \mu$m, which falls in the medium-wavelength infrared (MWIR) band. Thus, optical measurements of $\lambda < 1\ \mu$m using silicon sensors fall on the short-wavelength side of the Planck radiation curve. This curve falls off very steeply with decreasing wavelength below the peak of the thermal emissions, so the principal question to be addressed is whether enough energy from this part of the Planck curve intersects the sensor pass band to be detectable.

To understand the relation between camera sensitivity and wavelength in terms of a thermal emission spectrum, it is instructive to review the form of the Planck black-body radiation formula. The Planck formula for the spectral radiance $I(\lambda,T)$ of a black-body radiator in thermal equilibrium is (Rybicki and Lightman, 1979)

$$I(\lambda,T)=\frac{2hc^2}{\lambda^5}\frac{1}{e^{hc/\lambda k_B T}-1}, \qquad (1)$$

where λ is the wavelength in meters, T is temperature in Kelvins, $h = 6.63 \times 10^{-34}$ [J s] is Planck's constant, and $k_B = 1.38 \times 10^{-23}$ [J/K] is Boltzmann's constant. For a small wavelength interval $d\lambda$, the dimensions of $I(\lambda,d\lambda)d\lambda$ are energy flux per unit solid angle (in joules per square meter per second per steradian).

The Planck formula describes the black-body emissions for any temperature and wavelength. Emission contours illustrating the general features of the Planck formula over wavelengths and temperatures of interest to our observations are plotted in figure 3. For the present problem of detecting thermal radiation using silicon-based optical sensors sensitive in the wavelength range 400 to 1100 nm, nominal temperatures of 500 to 1,000°C (773 to 1273 K) for hot volcanic ejecta (Larsen 1929) correspond to a sensor response on the very steep short-wavelength side of the Planck curve. Here, the thermal-emission spectrum changes rapidly with wavelength and so is very sensitively dependent on the temperature. For example, near the range of temperatures under consideration, on the short-wavelength side of the Planck radiation curve a 10-percent decrease in wavelength produces an ~50-percent decrease in the flux density, whereas a 10-percent decrease in absolute temperature (127°C) produces an ~80-percent decrease in the flux density. The emissions therefore depend extremely sensitively on the emission temperature and wavelength, such that small calibration uncertainties are correspondingly magnified.

Imaging-System Response to Thermal Radiation

Imaging sensors detect quantized packets of energy in the form of photons, and so the energy flux at a given wavelength must be converted to to the equivalent photon flux. The energy (in joules) carried by a single photon is $E=h\nu=hc/\lambda$, so the photon flux corresponding to equation 1 is

$$P(\lambda,T)\,d\lambda=(\lambda/hc)I(\lambda,T)d\lambda, \text{ or}$$

$$P(\lambda,T)d\lambda=\frac{2c}{\lambda^4}\frac{1}{e^{hc/\lambda k_B T}-1}d\lambda, \qquad (2)$$

where $P(\lambda,T)d\lambda$ has the dimensions of photon flux per unit solid angle, (in protons per square meter per second per steradian).

The photon flux per unit wavelength incident on a pixel is then given by $N(\lambda,T)=P(\lambda,T)\,A\Omega$, where $N(\lambda,T)d\lambda$ is the number of photons per unit time in a small wavelength interval $d\lambda$ crossing a lens aperture of area A (in square meters) from a source region subtending a solid angle Ω (in steradians) as seen by an observer. The product $G=A\Omega$ (in square meters steradian) is the etendue (sometimes referred to as simply "A-omega") of the pixel-lens combination and is an important system element that determines the overall detected signal level.

For a circular lens of diameter D (in meters), the aperture area is $A=\pi D^2/4$ (in square meters). The aperture dimensions are not typically quoted for lenses used in imaging. Instead, this information is indirectly specified through the focal length L

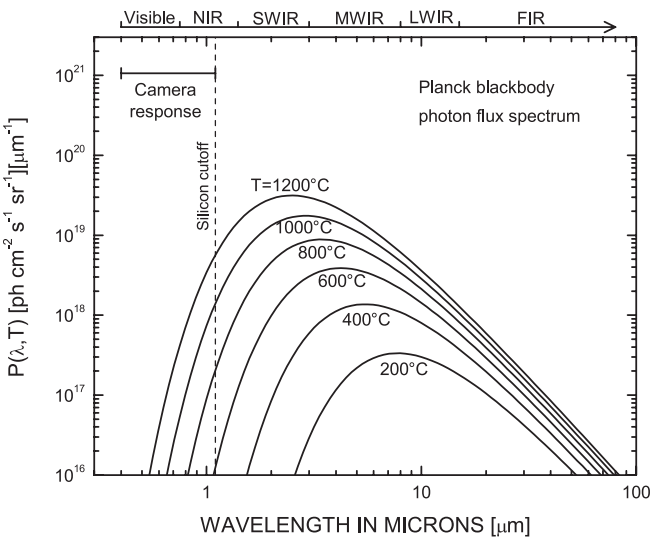

Figure 3. Photon flux spectrum $P(\lambda,T)$ for Planck blackbody radiation, expression (2) of the text. Note that here the unit area is expressed in cm^2 and the spectral density is in terms of mm^{-1}. The labels at the top refer to Near Infrared (NIR), Short Wavelength Infrared (SWIR), Medium Wavelength Infrared (MWIR), Long Wavelength Infrared (LWIR), and Far Infrared (FIR).

(commonly in mm), and the dimensionless speed (*f*-number) of the lens, where $f=L/D$, giving $A=\pi L^2/4f^2$.

For imagers where the focal plane of the lens is the CCD plane, the sensors are the individual pixels, and so the solid angle Ω subtended by the source is that of the field of view as seen by a single pixel. We assume that the source is of uniform brightness over the field of view of the pixel (diffuse-source approximation) and that the field of view is small, so angular apodization effects may be ignored. For a pixel of physical dimensions $p_x \times p_y$ (in square meters), the solid angle viewed by the pixel through a lens of focal length L is approximately $\Omega=p_x p_y / L^2$ (in sterdians).

Expressed in terms of the lens speed and pixel

dimensions, the etendue is $A\Omega=\frac{\pi}{4}\frac{p_x p_y}{f^2}$ (in square meters-steradians).

The number of blackbody photons per unit time incident on a pixel of dimensions $p_x \times p_y$ (in square meters) through a lens of speed *f* in a small wavelength interval $d\lambda$ centered on wavelength λ may then be written

$$N(\lambda,T)d\lambda = \frac{\pi c}{2\lambda^4}\frac{1}{\left(e^{hc/\lambda k_B T}-1\right)}\frac{p_x p_y}{f^2}d\lambda\ , \qquad (3)$$

which shows that for bare CCD imaging of diffuse sources, large pixel sizes and fast (small *f*-number) lenses are advantageous. We note that as expressed in equation 3, the physical area of the lens aperture, the focal length of the lens, and the solid angle of the source viewed by a single pixel are all implicitly contained in the ratio $p_x p_y / f^2$.

Atmospheric Transmission

The transmission of optical emissions through the atmosphere is highly susceptible to Rayleigh scattering, wavelength-dependent absorption from such atmospheric molecular species as water vapor, and absorption and Mie scattering from rain, snow, fog, aerosols, and dust. For observations through a large number of air masses over long horizontal distances, such as Augustine Volcano from Homer, Alaska, the transmissivity can vary widely and, in the absence of active calibrations that continuously monitor changing conditions, it can only be specified approximately. Typically, good observations were possible only on optically clear nights, but even under ideal conditions noticeable shimmering was evident in many images, possibly owing to refraction effects due to temperature gradients in the boundary layer, as well as to variations in the transmissivity from changing amounts of water vapor and aerosols. The level of shimmer in the images provided a useful gauge of boundary-layer stability.

To estimate the transmissivity of the atmosphere for the given viewing geometry, we computed a nominal transmissivity spectrum $S(\lambda)$ for the NIR wavelength range 0.7-1.5 μm using the U.S. Air Force Moderate Spectral Atmospheric Radiance and Transmittance code (MOSART) program, version 1.7. A horizontal pathlength of 105 km, corresponding to ~15 air masses, was assumed, with clean air and marine boundary-layer conditions. The model parameters used to calculate the atmospheric parameters were pressure, 10,135 Pa; temperature, 257.2 K; water vapor, 1,405 ppm by volume (ppmv) CO_2, 330 ppmv; ozone, 0.018 ppmv, N_2O, 0.32 ppmv and maritime aerosol conditions (from table 35, Subarctic (60° N) latitude winter atmosphere, "MOSART Model Atmospheres," Photon Research Associates, Inc., May 1993.)

The results are plotted in figure 4. Severe atmospheric absorption/attenuation bands are evident near ~0.76, 0.95, and 1.13 μm, and across a wide band of wavelengths 1.3 to 1.5 μm, which correspond to molecular absorption by water, and vary widely, depending on the overall pathlength and the air humidity. A general degradation in transmissivity from Rayleigh scattering occurs at wavelengths shorter than 0.7 μm. We propose that the observed bright emissions are from black-body radiation from hot Augustine ejecta and that the emissions are transmitted to the observation site through the relatively narrow atmospheric transmission band 1.0 to 1.1 μm.

The assumptions used for the transmissivity calculation represent ideal viewing conditions and omit the effects of fog or other types of atmospheric contaminant that frequently compromise viewing. The variability in atmospheric transmissivity due to changing weather conditions is the largest uncertainty in the interpretation of observations. The effective brightness temperature based on these assumptions is of only limited accuracy and should therefore be treated with appropriate caution.

Transmission Through the Optical Elements

Wavelength-dependent losses occur in various elements of the optical system, including the plexiglass window through which the camera viewed Augustine Volcano, and the camera lens. Calibrations were unavailable for these elements, and so a constant transmissivity of 0.5 was assumed for the window/lens combination.

Detector Response

The quantum efficiency as a function of wavelength, $R(\lambda)$, for the Sony ICX429ALL CCD sensor used in the camera is plotted in figure 5, where the normalized scale on the left corresponds to a maximum quantum efficiency of 70 percent at a wavelength of 600 nm. The manufacturer's data sheet does not extend beyond 1,000 nm, as shown, but it may be assumed the response continues to decrease uniformly to zero at the silicon cutoff at 1.1 μm. Most of the scene information in figures 1 and 2, including reflection of moonlight, stars, and evening sky brightness, comes from the main part of the sensitivity curve 400–700 nm. It is believed that the bright thermal emissions are being detected from the far right portion of the curve, at λ> 900 nm, where the quantum efficiency is very small (<5 percent). In this wavelength region, slight uncertainties in sensitivity can lead to large effects in the observed signal and the inferred temperature.

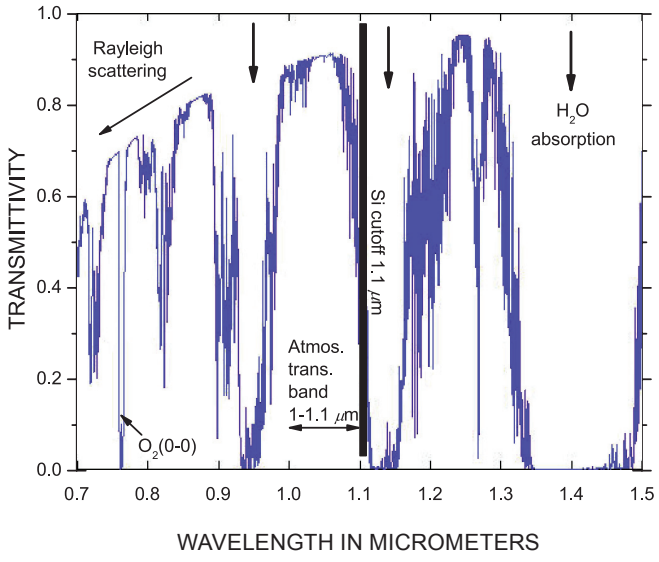

Figure 4. Atmospheric transmissivity versus wavelength 0.7-1.5 μm between Homer and Augustine volcano. The transmissivity was computed using MOSART code, assuming a horizontal path length looking through 15 air masses and marine boundary layer conditions. The heavy arrows at the top indicate major water- absoption bands, and the O_2(0-0) absorption line at 0.762 μm is also evident. The silicon cutoff wavelength at 1.1 μm is indicated. It is seen that there is a narrow transmission band between 1 and 1.1 μm.

End-to-End System Response Versus Black-Body Temperature

The photon counts from a thermal source accumulated over an integration interval of Δt is given by

$$N(T,\Delta t) = \Delta t \int_0^\infty N(\lambda,T) S(\lambda) R(\lambda) L(\lambda)\, d\lambda \ , \qquad (4)$$

where, from equation 3, the Planck formula for photon flux is

$$N(\lambda,T) = \frac{\pi c}{2\lambda^4} \frac{1}{(e^{hc/\lambda k_B T} - 1)} \frac{p_x p_y}{f^2} \ , \qquad (5)$$

in which we also include the etendue of the system. In equation 4, $S(\lambda)$ is the wavelength-dependent dimensionless atmospheric transmissivity function, and $R(\lambda)$ is the dimensionless CCD response function versus wavelength. Wavelength-dependent losses in the end-to-end transfer function of the optical train, given by $L(\lambda)$, include losses from lenses and filters, as well as from viewing ports such as glass or plexiglass windows. Additional factors that may be important for wide-angle scenes, but do not affect the present narrow field-of-view observations, include the apodization or obliquity factor needed to take into account the reduction in the apparent aperture area and pixel area for scene elements lying off the optical axis, and image vignetting that may occur if the physical size of the CCD detector is smaller than the image formed by the lens.

The photon counts into a pixel are given by the integral in equation 4, where the integrand is composed of four factors. On the short-wavelength side of the Planck spectrum near 1 μm the function $N(\lambda,T)$ increases rapidly with wavelength

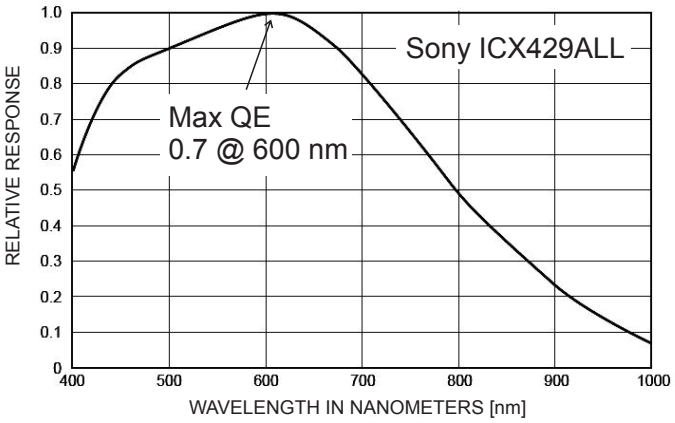

Figure 5. Relative response versus wavelength, normalized to the maximum quantum efficiency (QE), for the Sony model ICX429ALL CCD in the Starlight Xpress camera, per the Sony data sheet.

and temperature, while the sensor response $R(\lambda)$ decreases rapidly in this same wavelength region near the upper limits of its sensitivity. Their product, $P(\lambda,T)\ R(\lambda)$, is highly peaked around a wavelength of $\lambda \sim 1\ \mu$m and overlaps the atmospheric transmission window near 1 μm. The relations among these four factors are sketched in figure 6.

Given the overall uncertainties in the atmospheric transmissivity and detector sensitivity at wavelengths >1 μm, we use a crude approximation to estimate the value of the integral in equation 4. We assume that the integrand is highly peaked about some wavelength λ_0, as sketched in figure 6, that corresponds to transmission band $\lambda_0 \sim 1$ μm in figure 4. We further assume a width of the peaked function of $\Delta\lambda = 0.1$ μm, so that $\Delta\lambda << \lambda_0$. The integral may then be approximated using uniform response functions for $R(\lambda_0)$, $S(\lambda_0)$, and $L(\lambda_0)$. For a fixed geometry, the photon counts in a pixel as a function of source temperature and camera integration time is then

$$N(T,\Delta t) \approx \Delta t\, N(\lambda_0,T) R(\lambda_0) S(\lambda_0) L(\lambda_0)\, \Delta\lambda. \qquad (6)$$

Inserting system parameters for the present observations, we have: pixel dimensions of the Sony ICX429ALL CCD, 8.3 by 8.6 μm; relative response versus wavelength of the CCD (fig. 5), $\Delta\lambda = 0.1$ μm at $\lambda_0 = 1$ μm; quantum efficiency at $\lambda_0 = 1$ μm is ~0.01; lens speed $f/2.4$; integration time $\Delta t = 5$ s; atmospheric transmissivity $S(\lambda_0) = 0.8$; wavelength-dependent losses $L(\lambda_0) = 0.5$, which includes losses in the lens and from window absorption. With these parameters the expected number of pixel counts versus temperature T [°C] from thermal emissions is plotted in figure 7, where the curve labeled "Ideal emission spectrum" shows the pixel counts versus black-body source temperature for the assumed system parameters, and the dashed curves labeled "50%" and "25%" show the effects of including additional inefficiencies in the system. The recorded pixel counts of ~6,000 correspond to an apparent thermal temperature of 400 to 450°C for bright emissions.

Discussion

The observed emissions are consistent with thermal emissions at an apparent temperature of 400 to 450°C. With the given pixel resolution of several tens of meters at the source, each pixel would likely have included the combined effects of a heterogeneous mixture of hot emitters and cooler surfaces (Keszthelyi and others, 2003).

Although the emissions reported here were invisible to the unaided eye when spot checks were made at the time of the observations, other researchers reported incandescence during the eruption period that was visible through binoculars or when using color digital cameras and telephoto lenses. The human eye is generally insensitive to wavelengths longer than ~700 μm, even under dark-adapted conditions

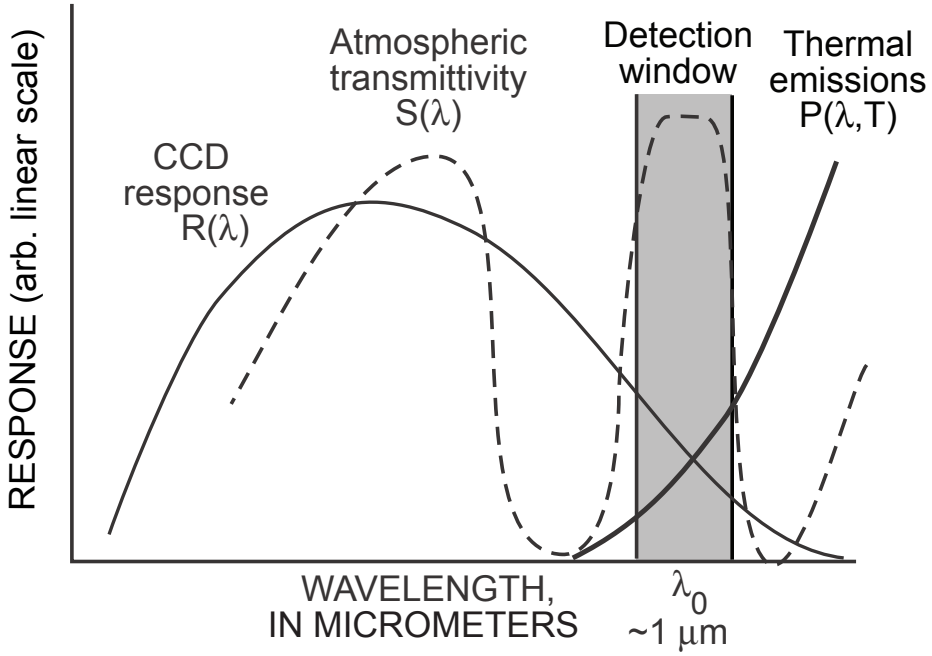

Figure 6. Sketch illustrating the various factors entering into the detectability of thermal emissions. The wavelength scale spans the general range of sensitivity of the camera CCD, from the blue on the left to the CCD cutoff wavelength slightly above 1 μm. The wavelength range believed detected in the images is indicated by the dark rectangle centered on $\lambda_0 \sim 1$ μm.

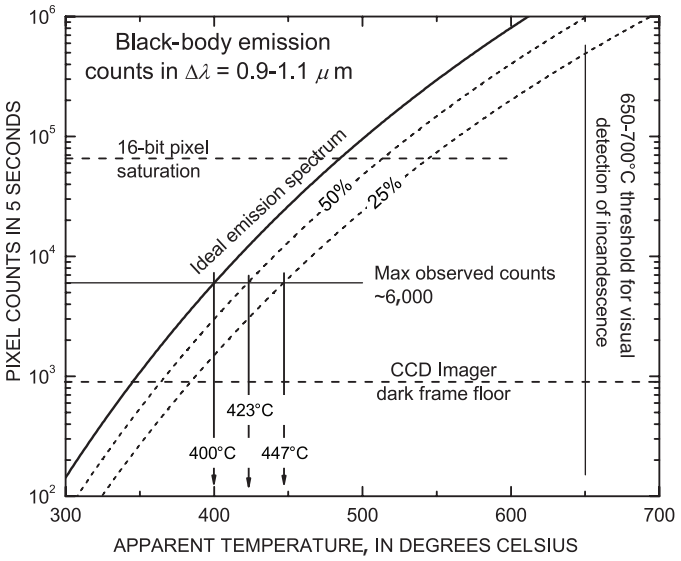

Figure 7. Number of counts in a 5 s integration interval for an f/2.4 lens and the system parameters given in the text. The heavy solid curve corresponds to the number of detector counts assuming an ideal black-body radiator at the given temperature on the abscissa. The effects on apparent temperature from departures from the ideal black-body due to additional inefficiencies beyond those assumed in the calculation are indicated by the dashed lines. The dark frame counts due to CCD thermal noise and bias are ~900 under typical operating conditions. The 16-bit saturation level is also shown. For the measured 6,000-count level shown, the apparent temperatures is ~400 to 450°C. The temperature threshold for visual detection of incandescence is indicated on the right.

(Kinney, 1958), so visual detection of incandescence implied that the temperatures at such times would have been at least ~650 to 700°C (see figure 7). We speculate that images of such visually detectable emissions made using the present camera system would have been much brighter than the examples presented here.

Conclusions

- Hot thermal emissions from steam releases, rockfalls, and pyroclastic flows from Augustine Volcano were detected in February to March 2006 using a small silicon-based astronomical camera. The observations were made over open water from a distance of ~105 km from Augustine.

- The emissions, which were quite bright in the optical images, were generally invisible to the dark-adapted human eye when spot checks were made, although informal observations of incandescence at other times were reported by other observers.

  Analysis of the emission brightness, taking into account the camera sensitivity versus wavelength and atmospheric transmissivity over the long distance between the volcano and the observing site, suggests that the detected emissions occurred within a narrow atmospheric-transmission window near the upper limit of the camera response at ~ 1 μm.

- The observed emissions are consistent with thermal emissions at an apparent temperature of 400 to 450°C. The uncertainties in this calculated apparent temperature are substantial because the observed emissions fall near the extreme limit of the camera response and the atmospheric transmissivity varies near this wavelength.

- Although silicon-based imagers are not optimal for detecting thermal emissions, the observations presented here suggest that they could provide a relatively inexpensive means to monitor some volcanoes for nocturnal thermal emissions.

Acknowledgments

We thank J. Dehn, J. Paskievitch, and K. Dean for useful discussions and D. Wilkinson for use of a camera lens. This work was supported by the Geophysical Institute University of Alaska Fairbanks, the Alaska Volcano Observatory, the U.S. Geological Survey as part of their Volcano Hazards Program, and by the State of Alaska.

References Cited

Calvari, S., Spampinato, L., Lodato, L., Harris, A.J.L., Patrick, M.R., Dehn, J., Burton, M.R., and Andronico, D., 2005, Chronology and complex volcanic processes during the 2002–2003 flank eruption at Stromboli volcano (Italy) reconstructed from direct observations and survey with a handheld infrared camera: Journal of Geophysical Research, v. 110, B02201, doi:10.1029/2004JB003129.

Dehn, J., Dean, K.G., Engle, K., and Izbekov, P., 2002. Thermal precursors in satellite images of the 1999 eruption of Shishaldin Volcano: Bulletin of Volcanology, v. 64, p. 507–519, doi:10.1007/s00445-002-0227-0.

DeRoin, N., McNutt, S.R., Reyes, C., and Sentman, D., 2007, Rockfalls at Augustine Volcano, Alaska—2003–2006: Eos (American Geophysical Union Transactions), v. 88, S43–1038.

Harris, A.J.L., Dehn, J., Patrick, M., Calvari, S., Ripepe, M., and Lodato, L., 2005, Lava effusion rates from handheld thermal infrared imagery; an example from the June 2003

effusive activity at Stromboli: Bulletin of Volcanology, v. 65, p. 101–117, doi: 10.1007/s00445-005-0425-7.

Jacobs, K.M., and McNutt, S.R., 2010, Using seismic *b*-values to interpret seismicity rates and physical processes during the preeruptive earthquake swarm at Augustine Volcano 2005–2006, *in* Power, J.A., Coombs, M.L., and Freymueller, J.T., eds., The 2006 eruption of Augustine Volcano, Alaska: U.S. Geological Survey Professional Paper 1769 (this volume).

James, M.R., Wilson, L., Lane, S.J., Gilbert, J.S., Mather, T.A., Harrison, R.G., and Martin, R.S., 2008, Electrical charging of volcanic plumes: Space Science Reviews, doi:10.1007/s11214-008-9362-z.

Keszthelyi, L., Harris, A.J.L., and Dehn, J., 2003, Observations of the effect of wind on the cooling of active lava flows: Geophysical Research Letters, v. 30, no. 19, p. 1989, doi:10.1029/2003GL017994.

Keszthelyi, L., Jaeger, W., Milazzo, M., Radebaugh, J., Davies, A.G., and Mitchell, K., 2007. New estimates for Io eruption temperatures—implications for the interior: Icarus, v. 192, p. 491–502.

Kinney, J.A.S., 1958, Comparison of scotopic, mesopic, and photopic spectral sensitivity curves: Journal of the Optical Society of America, v. 48, p. 185–190.

Larsen, E.S., 1929, The temperature of magmas: American Mineralogist, v. 14, p. 81–94.

McEwen, A.,Simonelli, D.P., Senske, D.R., Klaasen, K.P., Keszthelyi, L., Johnson, T.V., Geissler, P.E., Carr, M.H., and Belton, M.J.S., 1997. High-temperature hot spots on Io as seen by the Galileo Solid State Imaging (SSI) experiment: Geophysical Research Letters, v. 24, p. 2443–2446.

McEwen, A.S., Keszthelyi, L., Spencer, J.R., Schubert, G., Matson, D.L., Lopes-Gautier, R., Klaasen, K.P. , Johnson, T.V., Head, J.W., Geissler, P., Fagents, S., Davies, A.G., Carr, M.H., Breneman, H.H. and Belton, M.J.S., 1998, High-temperature silicate volcanism on Jupiter's moon Io: Science, v. 281, p. 87–90.

McNutt, S.R., and Davis, C.M., 2000, Lightning associated with the 1992 eruptions of Crater Peak, Mount Spurr Volcano, Alaska: Journal of Volcanology and Geothermal Research, v. 102, p. 45–65.

McNutt, S.R., and Williams, E.R., 2010, Volcanic lightning; global observations and constraints on source mechanisms: Bulletin of Volcanology, v. 72, p. 1153-1167, doi: 10.1007/s00445-010-0393-4.

Milazzo, M.P., Keszthelyi, L., Radebaugh, J., Davies, A.G., Turtle, E.P., Geissler, P., Klaasen, K.P., and McEwen, A.S., 2005, Volcanic activity at Tvashtar Catena, Io: Icarus, v. 179, p. 235–251.

Olson, J.V., Wilson, C.R., McNutt, S.R., and Tytgat, G., 2006, Infrasonic wave observations of the January 2006 Augustine Volcano eruptions: Eos (American Geophysical Union Transaction), v. 87, p. V51C–1685.

Patrick, M.R., Harris, A.J.L., Ripepe, M., Dehn, J., Rothery, D.A., and Calvari, S., 2007, Strombolian explosive styles and source conditions; insights from thermal (FLIR) video: Bulletin of Volcanology, v. 69, no. 7, p. 769–784, doi:10.1007/s00445-006-0107-0.

Power, J.A., and Lalla, D.J., 2010, Seismic observations of Augustine Volcano, 1970–2007, *in* Power, J.A., Coombs, M.L., and Freymueller, J.T., eds., The 2006 eruption of Augustine Volcano, Alaska: U.S. Geological Survey Professional Paper 1769 (this volume).

Radebaugh, J., McEwen, A.S., Milazzo, M.P., Keszthelyi, L.P., Davies, A.G., Turtle, E.P., and Dawson, D.D. , 2004, Observations and temperatures of Io's Pele Patera from Cassini and Galileo spacecraft images: Icarus, v. 169, p. 65–79.

Rybicki, G.B., and Lightman, A.P., 1979: Radiative processes in astrophysics: New York, Wiley-Interscience, 382 p.

Thomas, R.J., Krehbiel, P.R., Rison, W., Edens, H.E., Aulich, G.D., Winn, W.P., McNutt, S.R., Tytgat, G. and Clark, E. , 2007, Electrical activity during the 2006 Mount St. Augustine volcanic eruptions: Science, v. 315, no. 5815, p. 1097, doi:1126/science.1136091.

Thomas, R.J., McNutt, S.R., Krehbiel, P.R., Rison, W., Aulich, G., Edens, H.E., Tytgat, G, and Clark, E., 2010, Lightning and electrical activity during the 2006 eruption of Augustine Volcano, *in* Power, J.A., Coombs, M.L., and Freymueller, J.T., eds., The 2006 eruption of Augustine Volcano, Alaska: U.S. Geological Survey Professional Paper 1769 (this volume).

Williams, E.R., and McNutt, S.R., 2005, Total water contents in volcanic eruption clouds and implications for electrification and lightning, chap. 6 *of* Pontikis, C., ed., Recent progress in lightning physics: Kerala, India, Research Signpost Publishing, p. 81–93.